



Label-Free Nuclei Segmentation Using Intra-Image Self Similarity

Long Chen¹, Han Li^{2,3}, and S. Kevin Zhou^{1,2,3(✉)}

¹ Key Lab of Intelligent Information Processing of Chinese Academy of Sciences (CAS), Institute of Computing Technology, CAS, Beijing 100190, People's Republic of China

chenlong171@mails.ucas.ac.cn

² School of Biomedical Engineering, Division of Life Sciences and Medicine, University of Science and Technology of China, Hefei 230026, Anhui, People's Republic of China

hanli21@mail.ustc.edu.cn, skevinzhou@ustc.edu.cn

³ Center for Medical Imaging, Robotics, Analytic Computing and Learning (MIRACLE), Suzhou Institute for Advanced Research, University of Science and Technology of China, Suzhou 215123, Jiangsu, People's Republic of China

Abstract. In computational pathology, nuclei segmentation from histology images is a fundamental task. While deep learning based nuclei segmentation methods yield excellent results, they rely on a large amount of annotated images; however, annotating nuclei from histology images is tedious and time-consuming. To get rid of labeling burden completely, we propose a **label-free** approach for nuclei segmentation, motivated from one pronounced yet omitted property that characterizes histology images and nuclei: **intra-image self similarity (IIS)**, that is, within an image, nuclei are similar in their shapes and appearances. First, we leverage traditional machine learning and image processing techniques to generate a pseudo segmentation map, whose connected components form candidate nuclei, both positive or negative. In particular, it is common that adjacent nuclei are merged into one candidate due to imperfect staining and imaging conditions, which violate the IIS property. Then, we filter the candidates based on a custom-designed index that roughly measures if a candidate contains multiple nuclei. The remaining candidates are used as pseudo labels, which we use to train a U-Net to discover the hierarchical features distinguish nuclei pixels from background. Finally, we apply the learned U-Net to produce final nuclei segmentation. We validate the proposed method on the public dataset MoNuSeg. Experimental results demonstrate the effectiveness of our design and, to the best of our knowledge, it achieves the **state-of-the-art performances of label-free segmentation** on the benchmark MoNuSeg dataset with a mean Dice score of 79.2%.

Keywords: Label-free · Nuclei segmentation · Pseudo Label

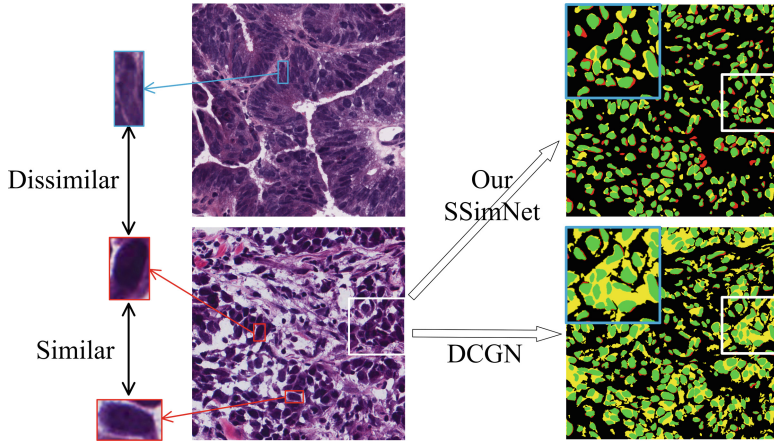


Fig. 1. The limitations of (deep) clustering model. Green, yellow and red colors refer to the true positive, the false positive and the false negative predictions. (Color figure online)

1 Introduction

Nuclei segmentation is a fundamental step in histology image analysis. In recent advances, with a large amount of labeled data, fully-supervised learning methods can easily achieve reasonable results [1–5]. However, accurate pixel-level annotation of nuclei is not always accessible for segmentation labeling is a labor-intensive and time-consuming procedure. Methods to relieve the high dependency on the accurate annotations of nuclei are highly needed.

Unsupervised learning (UL) methods achieved great success in the data dependency problem for nuclei segmentation, which learns from the structural properties in the data without any manual annotations. Based on the character of these methods, we can group them into two categories: the traditional UL methods and the deep learning UL methods. Traditional UL nuclei segmentation methods include watershed [6], contour detection [7], clustering [8,9] and random field [10]. These methods focus on either pixel value or shape information but fail to take advantage of both of them. Moreover, due to the heavily rely on preset parameters, these traditional methods also show weak robustness.

Therefore, some researchers [11–15] resort to deep UL segmentation models to better utilize both pixel value and shape information and develop a robust approach. The common and effective way is to employ image clustering by maximizing mutual information between image and predicted labels to distinguish foreground and background regions. Many image-clustering-based deep UL methods for natural tasks still achieve strong performances in nuclei segmentation. Kanezaki et al. [11] constrain a convolutional neural network (CNN) with super-pixel level segmentation results. Ji et al. [12] propose the invariant information clustering. While reasonable results are obtained, these deep clustering-based

methods still suffer difficulties: (i) Poor segmentation of the regions between adjacent nuclei. Deep clustering models succeed in transferring images to high-dimensional feature space and obtaining image segmentation results by means of clustering pixels' features. However, the regions between adjacent nuclei are similar to the nuclei regions in terms of color values and textures (as shown in Fig. 1). Deep clustering-based methods experience difficulties in dealing with these regions due to the lack of supervision. (ii) Underutilization of **intra-image self similarity (IISS)** information. As shown in Fig. 1, in terms of value, shape and texture, nuclei show a similar appearance within the same image but vary greatly among different images¹. This phenomenon offers valuable information for networks to use but the current clustering models do not take this into account.

To address the above issues and motivated by the IISS property, we hereby propose a novel self-similarity-driven segmentation network (**SSimNet**) for unsupervised nuclei segmentation. As shown in Fig. 2, instead of designing complex discriminative network architectures, our framework derives knowledge from the IISS property to aid the segmentation. Specifically, we obtain candidate nuclei with some unsupervised image processing. For the obtained candidates, it is common that adjacent nuclei merged into one candidate due to imperfect staining and low image quality, which violate the IISS property. Hence, we filter the candidates based on a custom-designed index that roughly measures if a candidate contains multiple nuclei. The remaining candidates are used as pseudo labels, which we use to train a U-Net (aka SSimNet) to discover the hierarchical features that distinguish nuclei pixels from the background. Finally, we apply the learned SSimNet to produce the final nuclei segmentation.

To validate the effectiveness of our method, we conduct extensive experiments on the MoNuSeg dataset [16, 17] based on ten existing unsupervised segmentation methods [9, 11–15, 18–20]. Our method outperforms all comparison methods with an average Dice score of 0.792 and aggregated Jaccard index of 0.498 on the MoNuSeg dataset which is close to the supervised method.

2 Method

As shown in Fig. 2, our SSimNet aims at unsupervised segmentation of nuclei from histology images. Specifically, by using a matrix factorization on hematoxylin and eosin (H&E) stained histology images, we get the hematoxylin channel image for clustering, active contour refining and softening to generate the final soft candidate label. Then according to the designed unsupervised evaluation metric driven from the IISS property, an SSimNet is trained with highly-rated soft pseudo labels and corresponding original patches. Last, while testing on the test image, to adapt the network to learn nucleus similarity within the same image, we fine tune the network with soft pseudo labels of some patches in current test images. In the following, we elaborate on each part in detail.

¹ Note that in our experiments, we use an image of size 1000^2 or 500^2 .

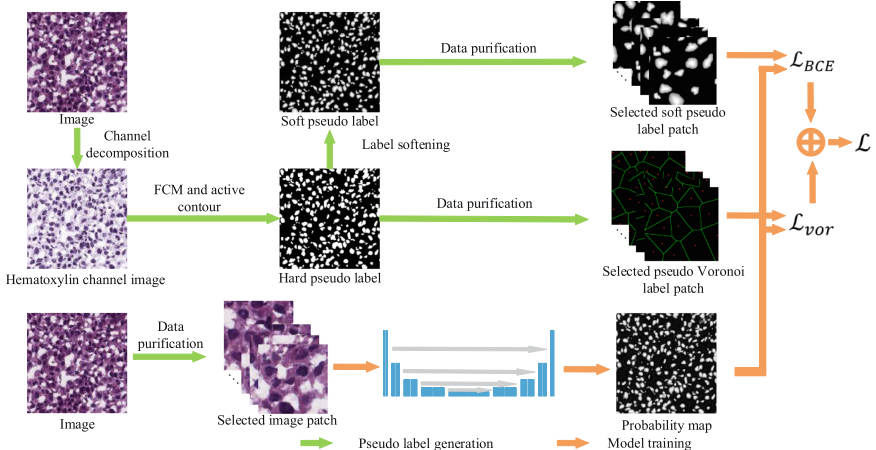


Fig. 2. The overview pipeline of the proposed method.

2.1 Candidate Nucleus Generation

Channel Decomposition. Suppose that we are given a training set $\mathcal{I}^S = \{I_i^S\}_{i=1}^N$ of histopathology images without any manual annotation. For each image, stained tissue colors are results from light attenuation, which depends on the type and amount of dyes that the tissues have absorbed. This property is prescribed by the Beer-Lambert law:

$$V = \log(I_0/I) = WH, \quad (1)$$

where $I \in \mathbb{R}^{3 \times n}$ represents the histology image with three color channels and n pixels, I_0 is the illuminating light intensity of sample with $I_0 = 255$ for 8-bit images in our cases, $W \in \mathbb{R}^{3 \times r}$ is the stain color matrix that encodes the color appearance of each stain with r representing the number of stains, and $H \in \mathbb{R}^{r \times n}$ is the stain density map. In this work, we follow the sparse non-negative matrix factorization in [21] to get the stain color matrices $\mathcal{W} = \{W_i\}_{i=1}^N$ and stain density maps $\mathcal{H} = \{H_i\}_{i=1}^N$ for \mathcal{I}^S . Note that usually histopathology images are stained with H&E and nuclei mainly absorb hematoxylin [22]; therefore, $r = 2$. We reconstruct the nuclei stain map with the first channel of \mathcal{W} and \mathcal{H} :

$$\mathcal{I}^T = \{I_i^T\}_{i=1}^N = \{W_i[:, 0] \cdot H_i[0, :] \}_{i=1}^N \quad (2)$$

Clustering and Active Contour. We transform \mathcal{I}^T into CIELAB color space and invoke the Fuzzy C-Means method (FCM) with 2 clusters to obtain the candidate foreground pixels. To reduce the noise in clustering results, we use active contour method as a smoothing operation to get hard candidate labels:

$$\mathcal{P} = \{P_i\}_{i=1}^N = \{\text{ActiveContour}(FCM(I_i^T))\}_{i=1}^N \quad (3)$$

Label Smoothing. Since hard label is overconfident at the border of nuclei, which is detrimental to the training of the network, we soften the hard label one by one for each connected component in P_i using the following formulation:

$$B[k+1] = B[k] + \frac{P[k]}{2 \cdot A} \quad (4)$$

where k represents the k^{th} epoch erosion of the connected component, $B[k]$ is the confidence score of pixels eroded in the k^{th} epoch and $B[0] = 0.5$ as the initial condition, $P[k]$ means number of pixels eroded in the k^{th} epoch, and A is the area of the connected component. As a terminal condition, we set the termination of erosion when $B[k] > 0.975$. Following Eq. (4), we obtain our soft candidate labels $\tilde{\mathcal{P}}$ from \mathcal{P} .

2.2 Data Purification and SSIMNet Learning

So far, soft candidate labels $\tilde{\mathcal{P}}_i$ have been acquired for each image I_i^S . However, it is common that adjacent nuclei are merged into one candidate due to imperfect staining and imaging conditions, which violate the IISS property. To this, we conduct data purification to build a reliable training set for subsequent learning.

Data Purification. We sample K patches with overlap from original image I_i^S . The sampled results are expressed as patch tissue $\mathcal{X} = \{x_i\}_{i=1}^{N \cdot K}$ and patch label $\mathcal{Y} = \{y_i\}_{i=1}^{N \cdot K}$. We design the Unsupervised Shape Measure Index (USMI) and calculate it using the algorithm in Fig. 3(left). Based on thresholding the USMI, we obtain pairs $(y_i, u_i)_{i=1}^{N \cdot K}$. Note that the smaller USMI is, the more the pseudo label conforms to prior knowledge. Sorting these pairs by USMI from the smallest to largest, only maintain the first $\alpha\%$ ($0 < \alpha < 100$) of data pairs as $(\tilde{\mathcal{X}} = \{x_{u(i)}\}_{i=1}^{\alpha \cdot N \cdot K}, \tilde{\mathcal{Y}} = \{y_{u(i)}\}_{i=1}^{\alpha \cdot N \cdot K})$. Figure 3(right) shows a separation of candidates into two groups (yellow and blue) with a typical yellow patch containing merger nuclei and a blue patch containing isolated nuclei.

To further separate possible adjacent nuclei in a blue patch, we follow [23] to construct the Voronoi label as in Fig. 2 by setting the center of connected component as 1, constructing Voronoi diagram, setting Voronoi edge as 0, and ignoring other pixels. Then, a Voronoi tri-label set $\tilde{\mathcal{Z}}$ can be acquired.

SSIMNet Learning and Finetuning. By denoting our segmentation network as F , our final loss function to supervise the network training can be formulated as:

$$\text{Loss} = \sum_{\tilde{x} \in \tilde{\mathcal{X}}, \tilde{y} \in \tilde{\mathcal{Y}}, \tilde{z} \in \tilde{\mathcal{Z}}} \lambda L_{BCE}(F(\tilde{x}), \tilde{y}) + (1 - \lambda) L_{CE}(F(\tilde{x}), \tilde{z}), \quad (5)$$

where L_{BCE} is the binary cross-entropy loss and L_{CE} is the cross-entropy loss.

Also, we can obtain tissue patches and corresponding pseudo labels for each image in the test set termed as $SET_k = (\tilde{\mathcal{X}}_k^T, \tilde{\mathcal{Y}}_k^T, \tilde{\mathcal{Z}}_k^T)$. Before evaluation, we first fine tune our network F using SET_k for several epochs. As shown in the ablation study, this operation is simple but effective. And this fine tuning process can help the network capture the size and shape information in the current test slice.

Algorithm 1 Computing Unsupervised Shape Measure Index(USMI)

Input: A set of connected component P_i indexed by i in the given segmentation label
Output: Unsupervised Shape Measure Index U

- 1: Initialize convex hull area sum and connected component count: $H \leftarrow 0; C \leftarrow 0$
- 2: Initialize list of connected component area: $A \leftarrow []$
- 3: **for** Each segmentation connected component P_i **do**
- 4: $C \leftarrow C + 1$
- 5: Compute the area and convex hull area of P_i as a_i and h_i
- 6: $A \leftarrow [A, a_i]; H \leftarrow H + h_i$
- 7: **end for**
- 8: Sort area value in A and only maintain the value between lower quartile(Q1) and upper quartile(Q3) in A and compute mean of A as \bar{A}
- 9: Compute $\bar{H} = H/C$
- 10: $U \leftarrow \bar{H}/\bar{A}$

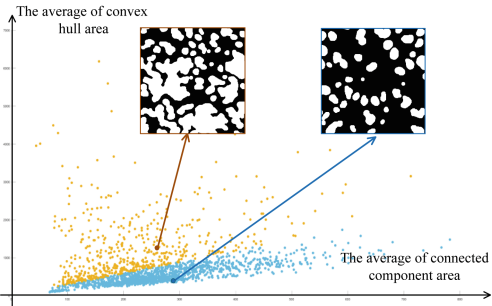


Fig. 3. Left: The algorithm that computes USMI. **Right:** Illustration of average convex hull area and the average of connected component area based on USMI. Yellow (or cyan) points denote the samples whose USMI is greater (or less) than the threshold. (Color figure online)

3 Experiments

3.1 Datasets and Settings

MoNuSeg. Multi-organ nuclei segmentation [16, 17] (MoNuSeg) is used to evaluated our SSIMNet. The MoNuSeg dataset consists of 44 H&E stained histopathology images with 28,846 manually annotated nuclei. With 1000×1000 pixel resolution, these images were extracted from whole slide images from the The Cancer Genome Atlas (TCGA) repository, representing 9 different organs from 44 individuals.

CPM17. The CPM17 dataset [24] is also derived from TCGA repository. The training and test set each consisted of 32 images tiles selected and extracted from a set of Non-Small Cell Lung Cancer (NSCLC), Head and Neck Squamous Cell Carcinoma (HNSCC), Glioblastoma Multiforme (GBM) and Lower Grade Glioma (LGG) tissue images. Moreover, each type cancer has 8 tiles and the size of patch is 500×500 or 600×600 .

Settings. We compare our SSIMNet with several current unsupervised segmentation methods. We follow the DCGN [15] to conduct comparison experiments. We crop the image in dataset into patches of 256×256 pixels for training. All the methods were trained for 150 epochs on MoNuSeg and 200 epochs on CPM17 each time and experimented with an initial learning rate of $5e^{-5}$ and a decay of 0.98 per epoch. Our experiment repeated ten times on MoNuSeg dataset and only once on CPM17 dataset for an augmented convenience. Specially for our SSIMNet training, we set $\alpha = 70\%$ for data purification and $\lambda = 0.9$ for loss in training. Moreover, we fine tune the network with only five epochs for each image on test set with optimizer parameter saved in checkpoint.

Table 1. Performance of the nuclei segmentation on MoNuSeg dataset. The best results are highlighted in **bold** and the second best underlined. ‘ft’ means fine tuning. The results are shown as “mean \pm standard deviation(upper-bound results)”.

Methods	Precision% \uparrow	Recall% \uparrow	Dice% \uparrow	AJI% \uparrow
mKMeans	65.7 \pm 17.5(67.9)	79.2 \pm 17.4(77.3)	67.8 \pm 9.4(68.2)	30.5 \pm 14.0(33.8)
GMM [9]	63.1 \pm 15.0(66.4)	82.2 \pm 10.9(81.9)	69.5 \pm 8.5(71.7)	29.0 \pm 15.1(31.9)
IIC [12]	46.7 \pm 9.2(51.6)	72.5 \pm 12.1(79.6)	56.0 \pm 8.7(61.8)	5.6 \pm 3.0(7.2)
Kim et al. [20]	57.5 \pm 24.9(69.8)	82.4 \pm 18.9(77.2)	60.6 \pm 17.1(69.4)	22.0 \pm 17.6(32.3)
Double DIP [18]	22.1 \pm 5.1(22.1)	82.0 \pm 10.9(85.1)	34.4 \pm 6.7(35.0)	1.3 \pm 0.6(1.3)
Kanezaki et al. [11]	62.9 \pm 19.5(72.5)	82.2 \pm 16.2(78.3)	66.9 \pm 11.9(72.7)	26.0 \pm 16.6(35.1)
DCGMM [14]	69.3 \pm 13.5(69.8)	78.6 \pm 17.1(80.1)	70.7 \pm 6.4(71.9)	31.4 \pm 12.4(34.5)
DIC [13]	51.1 \pm 24.9(59.5)	84.8 \pm 17.0(83.2)	57.1 \pm 16.5(64.4)	14.7 \pm 16.9(19.3)
DCAGMM [19]	61.9 \pm 13.7(69.1)	76.7 \pm 13.1(76.3)	66.4 \pm 7.9(70.6)	30.0 \pm 12.6(36.5)
DCGN [15]	68.5 \pm 11.3(71.6)	<u>83.4</u> \pm 11.5(80.8)	73.7 \pm 4.3(74.3)	35.2 \pm 11.3(37.9)
Our SSimNet w/o ft	<u>80.8</u> \pm 2.1(79.7)	76.1 \pm 3.3(79.3)	76.7 \pm 1.4(78.5)	<u>44.1</u> \pm 1.5(45.3)
Our SSimNet	82.0 \pm 1.7(82.0)	77.2 \pm 2.5(78.6)	79.2 \pm 0.6(80.0)	49.8 \pm 0.9(51.2)
U-Net (supervised)	73.8 \pm 1.3(75.5)	85.3 \pm 0.4(85.8)	78.7 \pm 1.0(80.0)	51.0 \pm 0.9(52.4)

3.2 Experimental Results

To evaluate the effectiveness of SSimNet, we compare it with several deep learning based and conventional unsupervised segmentation methods on the mentioned datasets, including minibatch K-Means (termed as mKMeans), Gaussian Mixture Model [9] (termed as GMM), Invariant Information Clustering [12] (termed as IIC), Double DIP [18], Deep Clustering via Adaptive GMM model [19] (termed as DCAGMM), Deep Image Clustering [13] (termed as DIC), Kim’s work [20], Kanezaki’s work [11], Deep Conditional GMM [14] (termed as DCGMM), and Deep Constrained Gaussian Network [15] (termed as DCGN). For the methods without public codes, we report the results from the original publications for a fair comparison. The results are shown in Table 1.

As Table 1 shows, firstly, our SSimNet outperforms all other unsupervised model and performs even close to fully supervised U-Net under the metrics of Dice coefficient and Aggregated Jaccard Index (AJI). Secondly, while the recall of all comparison methods is higher than precision, our SSimNet’s recall (0.772) is lower than precision (0.820) and also lower than the state-of-the-art method’s recall (0.834). The reason lies in that our method considers mining as strong prior knowledge from tissue slice itself, which renders a tighter constraint on our model, leading the model to predict a lower confidence in the easily-confused region. Moreover, Figure 4 shows the visualization of two test slice. It also conforms the effectiveness of our method on eliminating the model confusion in the region between adjacent nuclei and the ability in capturing nuclei shape.

Besides, we conduct an additional comparison experiment based on CPM17 dataset to demonstrate the generalization of our method. As shown in Table 2, our method again achieves the top performances. Moreover, as the image size of CPM17 is smaller than that of MoNuSeg, the performance gain is not as big as on the MoNuSeg dataset.

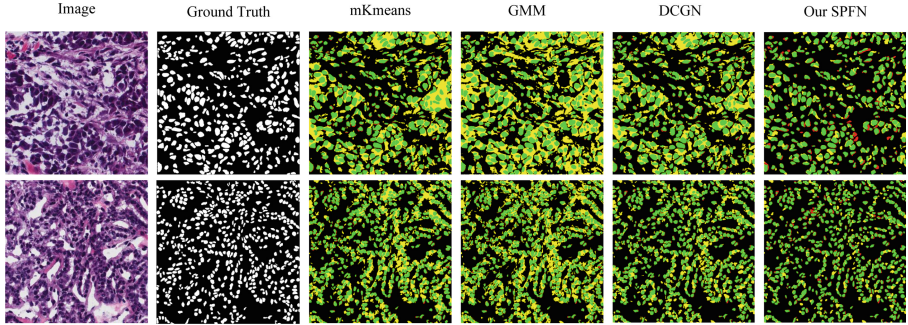


Fig. 4. Comparison of unsupervised nuclei segmentation results on MoNuSeg. Green, yellow and red colors refer to the true positive, the false positive and the false negative predictions. (Color figure online)

Table 2. Performance of the nuclei segmentation on CPM17 dataset. The best results are highlighted in **bold** and the second best underlined.

Methods	Precision%↑	Recall%↑	Dice%↑	AJI%↑
mKMeans	79.4	74.9	74.5	46.1
GMM [9]	79.0	75.5	72.7	43.0
Kanezaki et al. [11]	82.0	65.4	72.1	46.7
Our SSIMNet w/o finetune	<u>85.4</u>	80.7	<u>81.2</u>	<u>49.3</u>
Our SSIMNet	85.8	<u>80.5</u>	81.6	49.8

3.3 Ablation Study

We perform ablation studies by disabling each component to the SSIMNet framework to evaluate their effectiveness. As shown in Table 3, each component in our SSIMNet can bring different degrees of improvement, which shows that all of the label softening, data purification and finetuning process are significant parts of our SSIMNet and play an indispensable role in achieving superior performance.

Table 3. Ablation study on SSIMNet using MoNuSeg dataset.

LabelSoftening	DataPurification	Finetune	Precision%↑	Recall%↑	Dice%↑	AJI%↑
	✓	✓	78.8	78.7	78.3	45.6
✓		✓	79.6	77.3	77.9	47.6
✓	✓		80.8	76.1	76.7	44.1
✓	✓	✓	82.0	77.2	79.2	49.8

4 Conclusion

In this paper, we propose an SSimNet framework for label-free nuclei segmentation. Motivated by the intra-image self similarity (IISS) property, which characterize the histology images and nuclei, we design a series of operations to capture the prior knowledge and generate pseudo labels as supervision signal, which is used to learn the SSimNet for final nuclei segmentation. The IISS property renders us a tighter prior constraint for better model building compared to other unsupervised nuclei segmentation. Comprehensive experimental results demonstrate that SSimNet achieves the best performances on the benchmark MoNuSeg and CPM17 datasets, outperforming other unsupervised segmentation methods.

Acknowledgement. Supported by Natural Science Foundation of China under Grant 62271465 and Open Fund Project of Guangdong Academy of Medical Sciences, China (No. YKY-KF202206).

References

1. Graham, S., et al.: Hover-net: simultaneous segmentation and classification of nuclei in multi-tissue histology images. *Med. Image Anal.* **58**, 101563 (2019)
2. Graham, S., et al.: Mild-net: minimal information loss dilated network for gland instance segmentation in colon histology images. *Med. Image Anal.* **52**, 199–211 (2019)
3. Guo, Z., et al.: A fast and refined cancer regions segmentation framework in whole-slide breast pathological images. *Sci. Rep.* **9**(1), 882 (2019)
4. Mahbod, A., et al.: Cryonuseg: a dataset for nuclei instance segmentation of cryosectioned h&e-stained histological images. *Comput. Biol. Med.* **132**, 104349 (2021)
5. Xiang, T., Zhang, C., Liu, D., Song, Y., Huang, H., Cai, W.: BiO-Net: learning recurrent bi-directional connections for encoder-decoder architecture. In: Martel, A.L., et al. (eds.) MICCAI 2020. LNCS, vol. 12261, pp. 74–84. Springer, Cham (2020). https://doi.org/10.1007/978-3-030-59710-8_8
6. Umesh Adiga, P.S., Chaudhuri, B.B.: An efficient method based on watershed and rule-based merging for segmentation of 3-d histo-pathological images. *Pattern Recognit.* **34**(7), 1449–1458 (2001)
7. Wienert, S., et al.: Detection and segmentation of cell nuclei in virtual microscopy images: a minimum-model approach. *Sci. Rep.* **2**(1), 503 (2012)
8. Nogues, I., et al.: Automatic lymph node cluster segmentation using holistically-nested neural networks and structured optimization in CT images. In: Ourselin, S., Joskowicz, L., Sabuncu, M.R., Unal, G., Wells, W. (eds.) MICCAI 2016. LNCS, vol. 9901, pp. 388–397. Springer, Cham (2016). https://doi.org/10.1007/978-3-319-46723-8_45
9. Ragothaman, S., Narasimhan, S., Basavaraj, M.G., Dewar, R.: Unsupervised segmentation of cervical cell images using gaussian mixture model. In: Proceedings of the IEEE Conference on Computer Vision and Pattern Recognition Workshops, pp. 70–75 (2016)
10. Zhang, Y., Brady, M., Smith, S.: Segmentation of brain mr images through a hidden markov random field model and the expectation-maximization algorithm. *IEEE Trans. Med. Imaging* **20**(1), 45–57 (2001)

11. Kanezaki, A.: Unsupervised image segmentation by backpropagation. In 2018 IEEE International Conference on Acoustics, Speech and Signal Processing (ICASSP), pp. 1543–1547. IEEE (2018)
12. Ji, X., Henriques, J.F., Vedaldi, A.: Invariant information clustering for unsupervised image classification and segmentation. In: Proceedings of the IEEE/CVF International Conference on Computer Vision, pp. 9865–9874 (2019)
13. Zhou, L., Wei, W.: DIC: deep image clustering for unsupervised image segmentation. *IEEE Access* **8**, 34481–34491 (2020)
14. Zanjani, F.G., Zinger, S., Bejnordi, B.E., van der Laak, H.A.W.M., et al.: Histopathology stain-color normalization using deep generative models. In: Medical Imaging with Deep Learning (2018)
15. Nan, Y., et al.: Unsupervised tissue segmentation via deep constrained gaussian network. *IEEE Trans. Med. Imaging* **41**(12), 3799–3811 (2022)
16. Kumar, N., Verma, R., Sharma, S., Bhargava, S., Vahadane, A., Sethi, A.: A dataset and a technique for generalized nuclear segmentation for computational pathology. *IEEE transactions on medical imaging* **36**(7), 1550–1560 (2017)
17. Kumar, N., et al.: A multi-organ nucleus segmentation challenge. *IEEE Trans. Med. Imaging* **39**(5), 1380–1391 (2019)
18. Gandelsman, Y., Shocher, A., Irani, M.: “double-dip”: unsupervised image decomposition via coupled deep-image-priors. In: Proceedings of the IEEE/CVF Conference on Computer Vision and Pattern Recognition, pp. 11026–11035 (2019)
19. Wang, J., Jiang, J.: Unsupervised deep clustering via adaptive gmm modeling and optimization. *Neurocomputing* **433**, 199–211 (2021)
20. Kim, W., Kanezaki, A., Tanaka, M.: Unsupervised learning of image segmentation based on differentiable feature clustering. *IEEE Trans. Image Process.* **29**, 8055–8068 (2020)
21. Vahadane, A., et al.: Structure-preserving color normalization and sparse stain separation for histological images. *IEEE Trans. Med. Imaging* **35**(8), 1962–1971 (2016)
22. Feldman, A.T., Wolfe, D.: Tissue processing and hematoxylin and eosin staining. In: Histopathology: Methods and Protocols, pp. 31–43 (2014)
23. Hui, Q., et al.: Weakly supervised deep nuclei segmentation using partial points annotation in histopathology images. *IEEE Trans. Med. Imaging* **39**(11), 3655–3666 (2020)
24. Vu, Q.D., et al.: Methods for segmentation and classification of digital microscopy tissue images. *Front. Bioeng. Biotechnol.* **53** (2019)